Journal of Materials Chemistry A

Accepted Manuscript

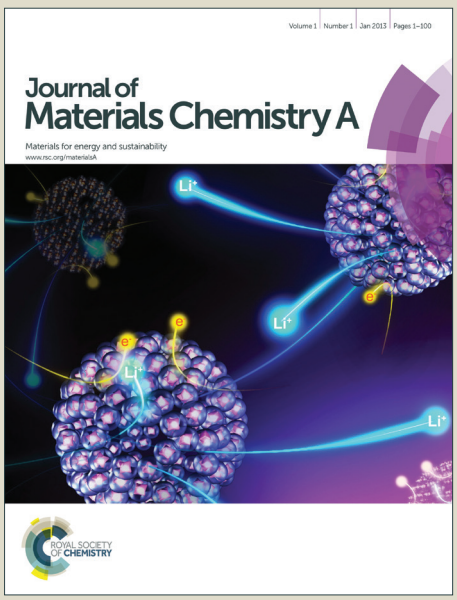

ROYAL SOCIETY OF CHEMISTRY

www.rsc.org/materialsA

Graphical Abstract

Lithium residues on the surface of $LiNi_{0.5}Co_{0.2}Mn_{0.3}O_2$ have been removed as raw materials to in-situ synthesize $LiAlO_2$-inlayed $LiNi_{0.5}Co_{0.2}Mn_{0.3}O_2$ cathode materials for lithium ion batteries.

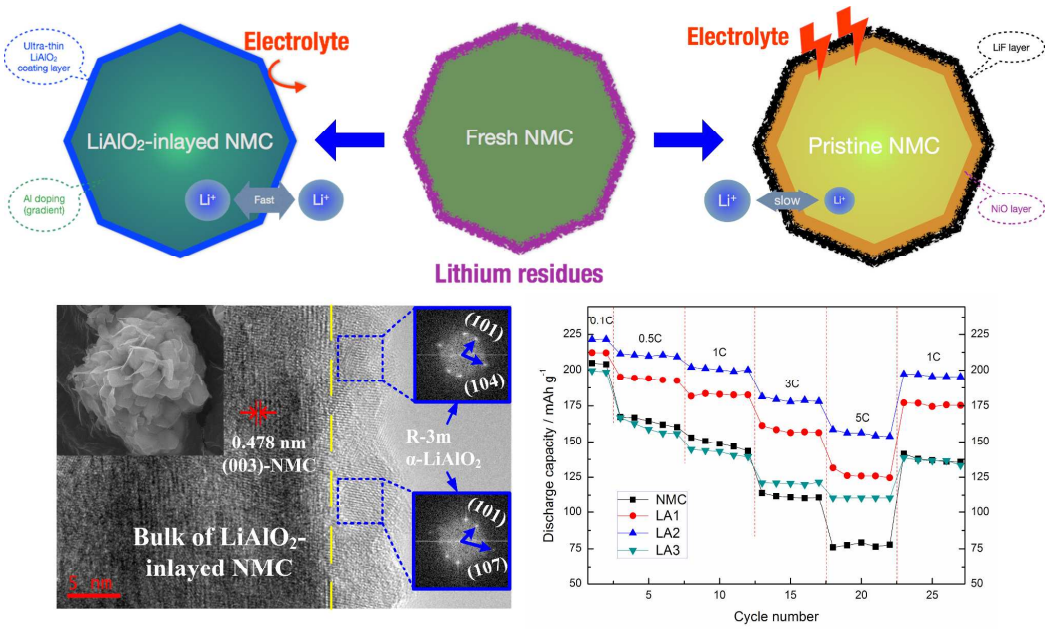

A Hydrolysis-Hydrothermal Route to Synthesis of Ultrathin $LiAlO_2$-inlayed $LiNi_{0.5}Co_{0.2}Mn_{0.3}O_2$ as High Performance Cathode Material for Lithium Ion Batteries

Lingjun Li[a, b], Zhaoyong Chen[a,*], Qiaobao Zhang[b], Ming Xu[a], Xiang Zhou[b], Huali Zhu[a], Kaili Zhang[b,*]

[a] *School of Physics and Electronic Science, Changsha University of Science and Technology, Changsha 410114, China*

[b] *Department of Mechanical and Biomedical Engineering, City University of Hong Kong, 83 Tat Chee Avenue, Kowloon, Hong Kong*

[*] Corresponding author: Kaili Zhang, Ph.D;
E-mail address: kaizhang@cityu.edu.hk
[*] Corresponding author: Zhaoyong Chen, Ph.D;
E-mail address: csullj@hotmail.com

Abstract: We have presented a novel hydrolysis-hydrothermal approach toward lithium residues on the surface of $LiNi_{0.5}Co_{0.2}Mn_{0.3}O_2$ as raw materials to synthesize ultrathin $LiAlO_2$-inlayed $LiNi_{0.5}Co_{0.2}Mn_{0.3}O_2$ cathode materials, for the first time. High resolution transmission electron microscopy (HRTEM) and Fast Fourier Transform (FFT) analysis indicate that the spherical particles of $LiNi_{0.5}Co_{0.2}Mn_{0.3}O_2$ are completely coated by crystalline $LiAlO_2$ with an average thickness of 4 nm, cross-section SEM and corresponding EDS results confirm that partial Al^{3+} ions are doped into the bulk $LiNi_{0.5}Co_{0.2}Mn_{0.3}O_2$ with gradient distribution. Electrochemical tests show that the modified materials exhibit excellent reversible capacity, enhanced cyclability and rate properties, combining with higher Li ions diffusion coefficient and better differential capacity profiles compared with those of the pristine one. Specially, the 2 mol% $LiAlO_2$-inlayed sample maintains 202 mAh g^{-1} with 91% capacity retention after 100 high-voltage cycles (with 4.6 V charge cut-off) at 1C. The enhanced electrochemical performance can be ascribed to the removal of lithium residues and the unique $LiAlO_2$-inlayed architecture. The removal of lithium residues are believed to decrease side reactions between Li_2O and electrolyte, while unique $LiAlO_2$-inlayed architecture can buffer the volume change of core and shell during cycles, enhance the lithium ion diffusion ability of composite and inherit the advantages of $LiAlO_2$ coating and doping.

Keywords:

$LiNi_{0.5}Co_{0.2}Mn_{0.3}O_2$; $LiAlO_2$; ultrathin inlaying; hydrolysis-hydrothermal; cathode

1. Introduction

Recently, the global warming and decreasing availability of fossil fuels are becoming more and more critical. To meet the demand for clean and sustainable energy, new generations of lithium ion batteries (LIBs) with higher energy density, longer cycling life, faster charging/discharging rate and better safety are highly required.[1-3] Layer-structured Ni-rich materials (Ni content ≥ 0.5), such as $LiNi_{0.5}Co_{0.2}Mn_{0.3}O_2$, $LiNi_{0.8}Co_{0.1}Mn_{0.1}O_2$ and $LiNi_{0.8}Co_{0.15}Al_{0.05}O_2$, have been considered as one of the most promising candidates to replace $LiCoO_2$ as cathode materials for LIBs and have been applied as key energy storage and conversion material in electric vehicles (Tesla), due to their high discharge capacity and low cost.[4-7]

Unfortunately, the wide practical use of the Ni-rich cathodes have so far been hindered by their weak interfacial stability between electrode and electrolyte,[8, 9] poor storage performance relates to high pH,[10, 11] high cation-mixing degree[12, 13] as well as low lithium ion diffusion coefficient. Cation substitution[14, 15] and surface coating[16-19] have been demonstrated as efficient approaches to enhance the electrochemical performance of Ni-rich materials.

For cation substitution, S. W. Woo et al.[14] found that Al, Mg substitution can restrain the cation-mixing degree and enhance the initial coulombic efficiency of cathodes. While, it is also noted that cathode materials still directly contact with electrolyte, and lithium ion diffusion coefficient has not been improved. For surface coating, it can act as "firewall" to prevent the active core material from directly contact with electrolyte and suppress the dissolution of metal ions.[20] However, the coating layers cannot decrease the cation mixing degree, and the different degrees of shrinkage within the same particle may lead to gradual separation of the core and shell, resulting in a drastic decline of battery performance.[5, 21] It is found that most modification technologies can only solve parts of problems and cannot improve the storage and C-rates performance of Ni-rich materials significantly. To reach high energy density from Ni-rich material, operation in the high cut-off voltage (≈4.5 V) is required, which inevitably places higher requirements for materials.[22, 23] Hence, some new and better modification architectures should be considered.

α-$LiAlO_2$ is typically layered material similar to the structure of Ni-rich materials.[24, 25] In addition, $LiAlO_2$ is electrochemical inert in a wide voltage range with excellent structural

stability in organic electrolyte.[26] Furthermore, $LiAlO_2$ possesses excellent lithium ion conductivity (up to 3×10^{-5} Ω^{-1} cm^{-1}) due to the partially occupied Li ion sites inside.[27] It is reported that Al-based doping is also conducive to the structural stability of Ni-rich cathode materials.[28, 29] In this regard, it is assumed that the presence of $LiAlO_2$ at the top surface and the bulk of host materials might help to improve the cycling stability as well as the rate capability of Ni-rich materials.

In view of synthesis routes, on the one hand, H. Cao et al.[30] have reported a sol-gel process to prepare $LiAlO_2$-coated $LiCoO_2$, and H.S. Kim et al.[31] produce $LiAlO_2$-coated $LiNi_{1/3}Co_{1/3}Mn_{1/3}O_2$ by the similar way. However, these methods cannot build a conformal, complete and ultrathin coating layer on the host materials. Because the lithium and aluminum sources are directly added into solution, the raw materials distribute randomly on the surface of host materials after drying, and the "coating" morphology takes place during calcination resulting in discontinuous and non-uniform coating layer. On the other hand, many reports indicate that excess lithium is necessary for synthesis of Ni-rich materials to perform optimally, and these excess lithium ions adhere on the particle surface in the form of Li_2O/LiOH, which could deteriorate the storage performance of Ni-rich materials and accelerate the decomposition process of $LiPF_6$.[32-34] While, it should be noted that these Li_2O/LiOH residues could also hydroxylize on the surface of the particle and be consumed as raw materials after suitable treatment. On this account, one can expect a kind of self-assembly approach between the hydroxyl (on particle surface) and coating material.

In this work, we first report a novel hydrolysis-hydrothermal approach for the successful preparation of a complete and ultrathin $LiAlO_2$-inlayed $LiNi_{0.5}Co_{0.2}Mn_{0.3}O_2$ cathode material. Lithium residues on the surface of $LiNi_{0.5}Co_{0.2}Mn_{0.3}O_2$ have been removed as raw materials to in-situ synthesize $LiAlO_2$-precursor coating layer. The formation of the "coating" morphology takes place during the hydrothermal step but not calcination. Moreover, the layered structure of α-$LiAlO_2$ is helpful for Al^{3+} ions diffusing into the bulk NMC during calcination. As expected, the thickness of $LiAlO_2$ coating layer is only 30~40 Å, and partial Al^{3+} ions are observed in the bulk $LiNi_{0.5}Co_{0.2}Mn_{0.3}O_2$ with gradient distribution. Compared with traditional structures, this unique inlayed architecture can buffer the volume change of core and shell during cycles, enhances the lithium ion diffusion ability of composite and inherits the advantages of $LiAlO_2$

coating and doping. The optimized $LiAlO_2$-inlayed sample delivers a high discharge capacity of 202 mAh g^{-1} (1C) with 91% capacity retention after 100 cycles at a large cut-off potential of 4.6 V.

2. Experimental

2.1 Materials synthesis

Spherical $LiNi_{0.5}Co_{0.2}Mn_{0.3}O_2$ layered materials are synthesized by solid-state reaction using Li_2CO_3 (99.9%, Kernel, Tianjin) and commercial transition-metal hydroxide precursors $(Ni_{0.5}Co_{0.2}Mn_{0.3})(OH)_2$ as raw materials. The precursor is mixed thoroughly with excess Li_2CO_3 in a molar ratio of 2:1.05. The mixture is heated at 480 ^oC for 5 h then calcined at 880 ^oC for 12 h in air at a heating rate of 5 ^oC min^{-1}.

$LiAlO_2$-inlayed $LiNi_{0.5}Co_{0.2}Mn_{0.3}O_2$ compounds, labeled as (NMC) 0 mol% $LiAlO_2$, (LA1) 1 mol% $LiAlO_2$, (LA2) 2 mol% $LiAlO_2$, and (LA3) 3 mol% $LiAlO_2$, are synthesized by a two-step process. (1) Hydrolysis process: An appropriate amount of aluminum isopropoxide powders are dissolved into 60 mL absolute ethanol, followed by addition of 50 mL mixture of deionized water and absolute ethanol. The mixture is maintained at 60 ^oC under stirring for 4 hours to form a sol. Afterward, the $LiNi_{0.5}Co_{0.2}Mn_{0.3}O_2$ powders are added into the sol and stirred for 0.5 h. (2) Hydrothermal process: The mixture is transferred into a Teflon-lined autoclave and kept at 150 ^oC for 15 h. The product is washed with de-ionized water and ethanol for several times and dried in an oven at 80 ^oC for more than 2 h, which is labeled as (LAH1) 1 mol% Al, (LAH2) 2 mol% Al, and (LAH3) 3 mol% Al, respectively. Then, the blend is collected and calcined at 500 ^oC for 4 h in air with a heating rate of 3 ^oC min^{-1} to obtain the $LiAlO_2$ nanosheet inlayed $LiNi_{0.5}Co_{0.2}Mn_{0.3}O_2$.

2.2 Materials characterizations

The phase of all samples is identified by X-ray diffraction (XRD, Rigaku D/Max 200PC, Japan) using Cu Kα radiation. The scanning rate is 5° min^{-1} and the scanning range of diffraction angle (2θ) is 10° ~ 90°. The morphologies and microstructures of all samples are analyzed by scanning electron microscopy (SEM, Nova NanoSEM-230), and high resolution transmission electron microscopy (HRTEM, FEI Tecnai G2 F20 S-Twin working at 200kV). Also, energy dispersive X-ray spectroscopy (EDS) is carried out on OXFORD 7426 as the attachment of SEM, with the acceleration voltage of 20 kV.

2.3 Electrochemical measurement

CR2025 coin-type cells are applied for electrochemical test. Typical positive electrode loadings are in the range of 1.95 − 2 mg cm^{-2}, and an electrode diameter of 14 mm is used. Cathode disks are pressed in a hydraulic press to 15 Mpa. The cathode consists of 85 wt. % active material, 10 wt. % acetylene black and 5 wt. % PVDF binder. A lithium metal foil is used as anode. $LiPF_6$ (1 M) in a 1:1:1 (v/v/v) mixtures of dimethyl carbonate (DMC), Ethyl Methyl Carbonate (EMC) and ethylene carbonate (EC) is used as electrolyte. The assembly of the cells is carried out in a dry Ar-filled glove box. Electrochemical tests are carried out using an automatic galvanostatic charge-discharge unit, Land CT2001 battery cycler, between 2.7 and 4.4/4.6 V versus Li/Li^+ electrode at room temperature. The electrochemical impedance spectroscopy (EIS) measurements are conducted by a CHI660a impedance analyzer, using 2-electrode cells. The amplitude voltage is 5 mV and frequency range is 10^{-3} − 10^{-1}MHz.

3. Results and discussion

It has been reported that $LiAlO_2$ crystallizes with three structures, the hexagonal α-$LiAlO_2$, monoclinic β-$LiAlO_2$ and tetragonal γ-$LiAlO_2$.[25, 26] In order to confirm the possible formation of α-$LiAlO_2$ by hydrolysis-hydrothermal process, an appropriate amount of $LiOH{\cdot}H_2O$ have been added into the AlO(OH) sol to replace the NMC particles and to process hydrothermal treatment. After drying at 80 °C and heating at 500 °C for 4 h, the powders show clear crystallinity of α-$LiAlO_2$ phase (JCPDS no. 74-2232), while the minor peak corresponds to β-$LiAlO_2$ phase (JCPSD no. 33-0785) as shown in Fig. 1a. TEM image in Fig. 1b further reveals the synthesized α-$LiAlO_2$ displays ultrathin nanosheets micrograph.

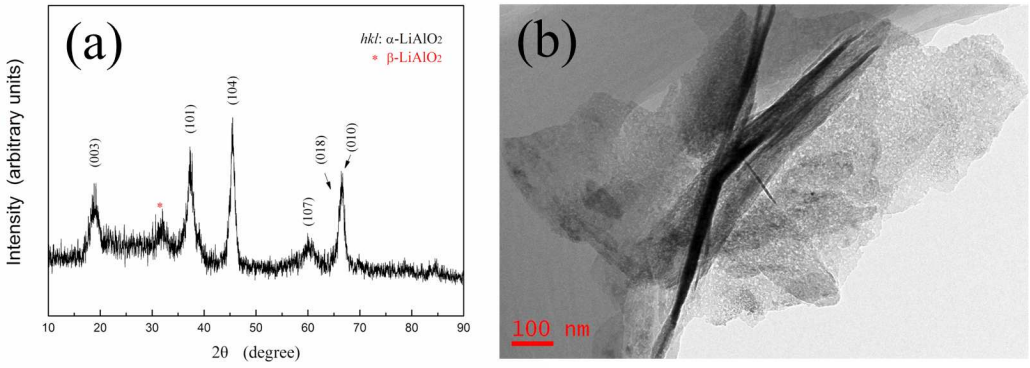

Fig. 1 XRD pattern of (a) $LiAlO_2$ nanosheets after heat treatment at 500 °C for 4 h and (b) corresponding TEM image.

The schematic illustration for the synthetic process of $LiAlO_2$ inlayed $LiNi_{0.5}Co_{0.2}Mn_{0.3}O_2$ material is shown in Fig. 2. The pH value of fresh NMC is 12.2, tested by adding 100 g powders into 1L deionized water. The concentration of Li^+ in water $C(Li^+)$ is approximately equal to $C(OH^-)$ and could be calculated from pH value. Assuming that the surface lithium residues rather than chemical delithiation of bulk contribute to this pH value, the molar of residual Li (n_{Li}) is equal to $C(Li^+) \times 1$ L, and the molar ratio of residual Li could be calculated by $n_{Li} \times M_{NMC}/100$. It is found that about 1.53 mol% Li^+ ions adhere on the interface of the NMC particles, so, we choose 1 mol%, 2 mol% and 3 mol% of $C_9H_{21}O_3Al$ (the molar ratio of NMC is 100%) to perform the hydrolysis process. A solution of deionized water and absolute ethanol is added to control the reaction speed of hydrolysis and achieve $Al(OH)_3$ sol. The detailed chemical mechanisms of this reaction are presented as following.[35]

$$Al(OC_3H_7)_3 + H_2O \xrightarrow{Hydrolysis} Al(OC_3H_7)_2(OH) + C_3H_7OH \quad (1)$$

$$2Al(OC_3H_7)_2(OH) + H_2O \xrightarrow{Hydrolysis} Al_2O(OC_3H_7)_2(OH)_2 + 2C_3H_7OH \quad (2)$$

$$Al_2O(OC_3H_7)_2(OH)_2 + H_2O \xrightarrow{Hydrolysis} 2AlO(OH) + 2C_3H_7OH \quad (3)$$

$$AlO(OH) + H_2O \xrightarrow{Hydrolysis} Al(OH)_3 \quad (4)$$

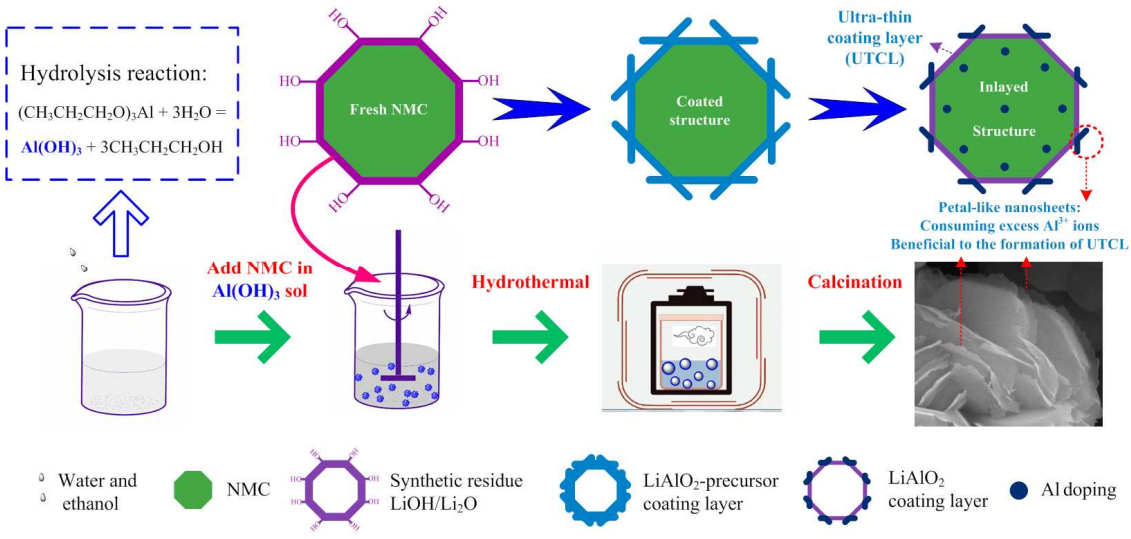

Fig. 2 Schematic diagram of the synthesis process for ultrathin $LiAlO_2$-inlayed $LiNi_{0.5}Co_{0.2}Mn_{0.3}O_2$ composite.

Then $LiNi_{0.5}Co_{0.2}Mn_{0.3}O_2$ powders are added into the sol with constant stirring. The $Al(OH)_3$ sol might migrate on the surface of NMC powders to form uniform coating layer, which is driven by thermodynamic force to reduce the structure's total surface energy.[36] The Li_2O residues could be hydroxylized at the same time. Afterward, the mixture is transferred into a Teflon-lined autoclave to capture $Al(OH)_3$, and a $LiAlO_2$-precursor coating layer is formed. At last, an annealing treatment is carried out, and partial Al^{3+} ions diffuse into the bulk $LiNi_{0.5}Co_{0.2}Mn_{0.3}O_2$ due to the similar structural between NMC and $LiAlO_2$, and the $LiAlO_2$-inlayed composite is attained. The chemical reaction occurring in the system is:[37]

$$Li_2O + H_2O \longrightarrow 2LiOH \quad (5)$$

$$Al(OH)_3 + LiOH + H_2O \xrightarrow{Hydrothermal} LiAl(OH)_4 \cdot H_2O \quad (6)$$

$$LiAl(OH)_4 \cdot H_2O \xrightarrow{500^oC} \alpha - LiAlO_2 + 3H_2O \quad (7)$$

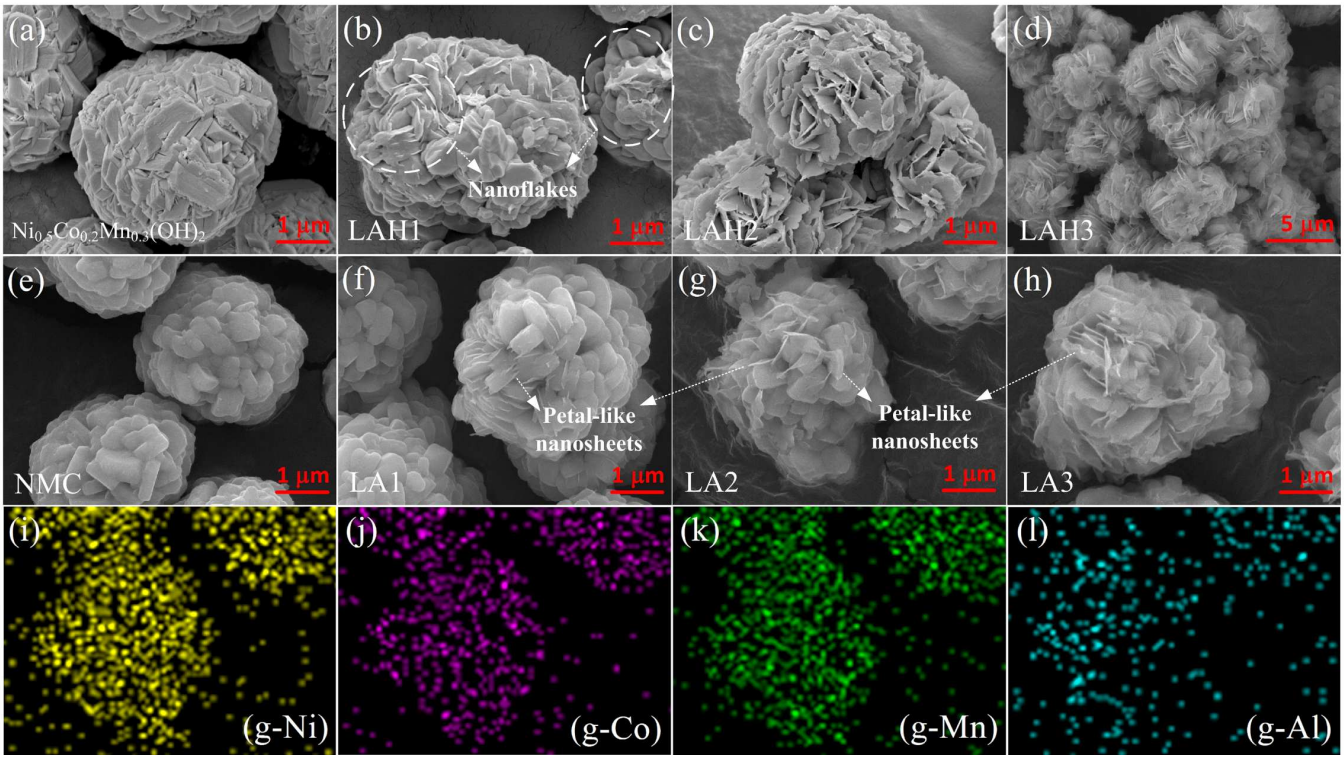

Fig. 3 SEM images of the $Ni_{0.5}Co_{0.2}Mn_{0.3}(OH)_2$, pristine and Al compounds coated $LiNi_{0.5}Co_{0.2}Mn_{0.3}O_2$ powders: (a) $Ni_{0.5}Co_{0.2}Mn_{0.3}(OH)_2$, (b − d) LAH1, LAH2, and LAH3, (e) NMC, and (f − h) LA1, LA2, and LA3; (i − l) EDS mapping of the LA2 based on (g).

The SEM images of $Ni_{0.5}Co_{0.2}Mn_{0.3}(OH)_2$, NMC, LAH1 − LAH3, and LA1 − LA3 are shown in Fig. 3. As can be seen, little morphology difference could be found between the $Ni_{0.5}Co_{0.2}Mn_{0.3}(OH)_2$ (Fig. 3a) and pristine $LiNi_{0.5}Co_{0.2}Mn_{0.3}O_2$ (Fig. 3e), the secondary particles show uniform spherical images, and the average particle size is 600 nm. Fig. 3b−d show the SEM images of the $LiAlO_2$-precursor coated $LiNi_{0.5}Co_{0.2}Mn_{0.3}O_2$, considering that the concentration of Al^{3+} ions is more than that of Li^+ ions for some sample, the $LiAlO_2$-precursor might include both $LiAl(OH)_4 \cdot H_2O$ and $Al(OH)_3$. With the increase of Al concentration, $LiAlO_2$-precursor nanoflakes appear on the surface of spheres (Fig. 3b) and grow up to form flower-like structures (Fig. 3c and d) until Al ions are totally consumed.

After being calcined at 500 ^oC, the $LiAlO_2$-precursor nanoflakes are transformed into petal-like nanosheets and ultrathin coating layer due to dehydration, as shown in Fig. 2 and Fig. 3(f − h). For the LA2 (Fig. 3g), Al^{3+} ions are covered on the particle surface completely (Fig. 3l), and excess Al^{3+} ions are accumulated on the petal-like nanosheets, which is supposed to have little influence on the thickness increase of coating layer and could retard the erosion of electrolyte. For the LA1 (Fig. 3f), the distribution of nanasheets is non-uniform due to low concentration of Al^{3+} ions. While, for the LA3 (Fig. 3h), those petal-like nanosheets grow thicker and wider, which even completely cover the bulk NMC and increase the transportation length of Li^+-ion. Moreover, during the experiment we find there is only small difference on the morphology between the LAH and LA samples, which indicates the formation of the "coating" morphology should take place during hydrothermal step but not calcination. As a result, with the hydrolysis-hydrothermal process, petal-like nanosheets coated composites are successfully synthesized, and the LA2 owns the superior micro morphology.

To study the morphology and microstructure of the potential ultrathin coating layer, HRTEM and corresponding FFT (Fast Fourier Transform) are performed for the pristine, 2 mol% and 3 mol% $LiAlO_2$-inlayed materials. As seen in Fig. 4, the pristine sample (Fig. 4a) shows fuzzy surface, K. Shizuka[38] and G.V. Zhuang[39] report that excess lithium is not in the crystal but on the surface. Hence, it is reasonable to think the fuzzy surface is Li_2O/LiOH layer. The FFT pattern and lattice fringes in the internal region of NMC and LA2 reveal that the $LiNi_{1-x-y}Co_xMn_yO_2$ phase is successfully formed. Compared with the pristine sample, the LA2 (Fig. 4b, Fig. 4c) exhibits conformal ultrathin coating layers with 30~40 Å thickness, and the

lattice fringes of the coating layers have interplannar distances of 4.73 Å, which corresponds to the d-spacing of the (003) planes of α-$LiAlO_2$ (JCPDS no. 74-2232). In addition, the FFTs in Fig. 4c also exhibit a α-$LiAlO_2$ type layered phase (space group $R\bar{3}m$). Moreover, considering that the structure of $LiAlO_2$ resembles that of NMC, a comparison experiment (as shown in the Supporting Information, Fig. S1) has been performed to further prove that the NMC cannot form coating layer via the same hydrothermal and calcination process. Therefore, it could be concluded that a crystalline and ultrathin α-$LiAlO_2$ coating layer has been established, which is consistent with the analysis in Fig. 1a.

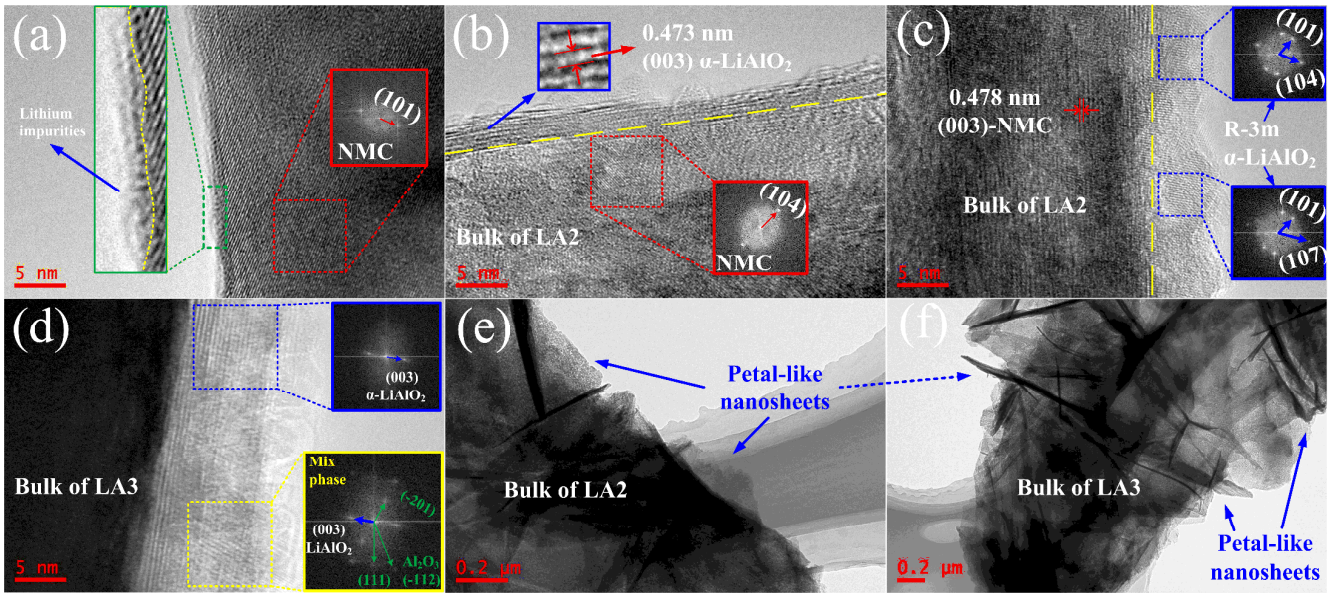

Fig. 4 HRTEM and corresponding FFT (Fast Fourier Transform) images of (a) pristine, (b, c) LA2 and (d) LA3 powders, and TEM images of (e) LA2 and (f) LA3 powders.

For the LA3 (Fig. 4d), the thickness of coating layer is about twice than that of the LA2. Beside, the corresponding FFTs show two sets of reflections that could very refer to the α-$LiAlO_2$ structure and Al_2O_3 structure (JCPDS no. 86-1410), which are mixing with one another at the atomic level. These results confirm the assumption that partial Al_2O_3 appear on the particle surface and increase the thickness of coating layer due to high concentration of Al^{3+} ions. The TEM of LA2 and LA3 are shown in Fig. 4e and f, respectively. The $LiAlO_2/Al_2O_3$ nanosheets completely coat on the bulk NMC and extend beyond the particle surface to form petal-like architectures, which are consistent with TEM and SEM images in Fig. 1b and Fig. 3.

These all can demonstrate that $LiAlO_2$ layer grows along flat surface resulting in ultrathin coating layer and petal-like nanosheets during hydrolysis-hydrothermal approach.

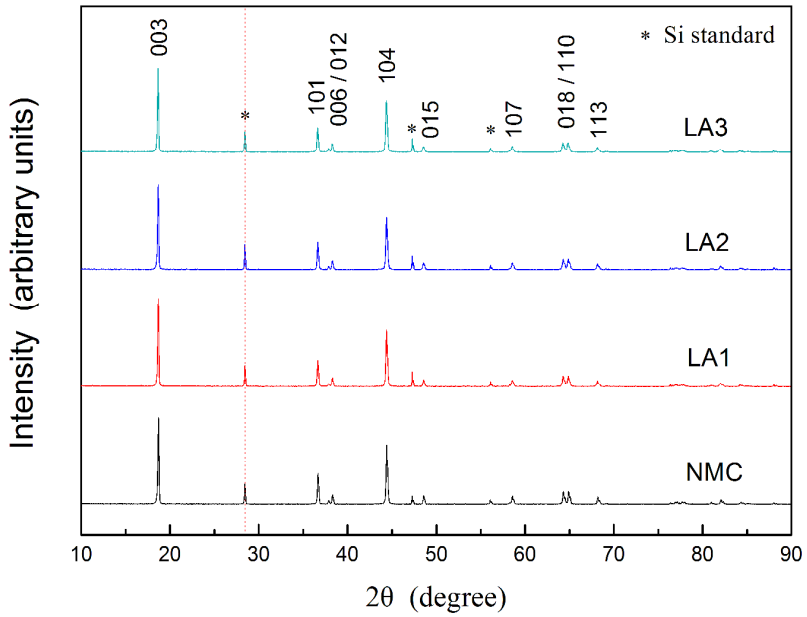

Fig. 5 Calibrated XRD patterns of pristine and $LiAlO_2$-inlayed $LiNi_{0.5}Co_{0.2}Mn_{0.3}O_2$ samples with Si standard.

Table 1 Lattice constants of pristine and $LiAlO_2$-inlayed $LiNi_{0.5}Co_{0.2}Mn_{0.3}O_2$ samples.

Sample	Lattice parameters	
	a (Å)	c (Å)
NMC	2.8747	14.2128
LA1	2.8748	14.2263
LA2	2.8741	14.2360
LA3	2.8745	14.2462

To clearly confirm the influence of $LiAlO_2$ inlaying on NMC structure, the prepared samples are mixed thoroughly with Si standard (JCPSD no. 27-1402) in a mass ratio of 9:1. The calibrated XRD patterns of the pristine and $LiAlO_2$-inlayed samples are exhibited in Fig. 5. All the diffraction lines are indexed on the Si standard and the rhombohedral α-$NaFeO_2$ structure with a space group of $R\bar{3}m$. The distinct splitting of (006)/(012) and (018)/(110) indicates the well-developed layered structure. However, third phase is not detected, which can be ascribed to the similar layered structure of $LiAlO_2$ and low concentration of Al_2O_3 phase. The lattice

constants of all samples are shown in Table 1. It is noted that the lattice parameter *c* increases with $LiAlO_2$ inlaying. This suggests that Al is highly possible to dope into bulk $LiNi_{0.5}Co_{0.2}Mn_{0.3}O_2$.[14]

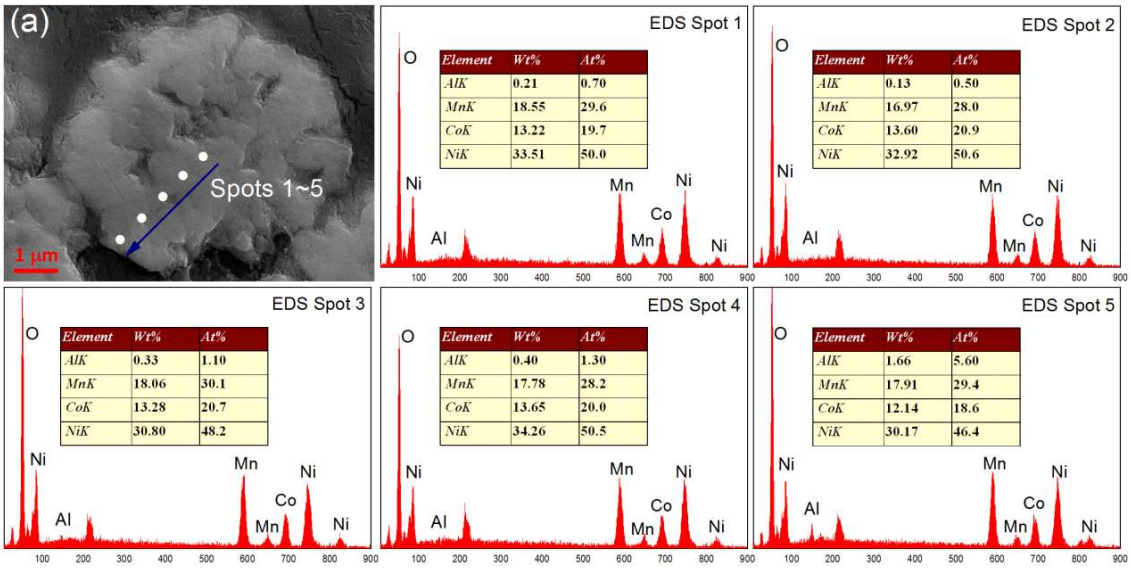

Fig. 6 EDS compositional change from the cross-section of LA2 particle.

Fig. 6 shows the cross-section SEM image of LA2 particle and its corresponding EDS results. Five spots, from the core center to outer layer (named spot 1~5 respectively), have been chosen to investigate the inner composition change of the $LiAlO_2$-inlayed sample. It is noted that the molar ratio of Ni, Co and Mn is close to the stoichiometry and remains almost constant from the spot 1 to 5, which confirms the bulk is $LiNi_{0.5}Co_{0.2}Mn_{0.3}O_2$. Besides, trace Al is observed in the core center, and the concentration of Al increases slowly from spot 1 to 4. This should be ascribed to mass diffusion of Al during the calcinations process, as $LiAlO_2$ is layered structure similar to that of NMC. For the spot 5, the concentration of Al increases sharply from 1.3 at% to 5.6 at%, while a considerable amount of Ni, Co and Mn are also found in shell, which might be ascribed to the ultrathin thickness of $LiAlO_2$ coating layer and the limitation of EDS analysis. Based on those EDS results, we find most Al^{3+} ions accumulate on the outer layer of particle, while partial Al^{3+} ions dope into the buck $LiNi_{0.5}Co_{0.2}Mn_{0.3}O_2$ with a gradient distribution. Thus the $LiAlO_2$-inlayed $LiNi_{0.5}Co_{0.2}Mn_{0.3}O_2$ composite is confirmed.

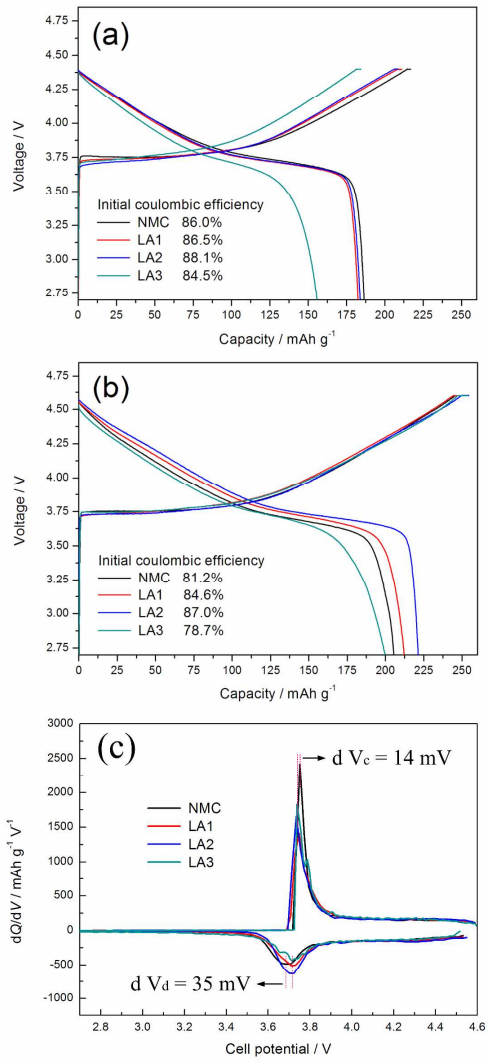

Fig. 7 Initial charge-discharge curves of pristine and $LiAlO_2$-inlayed $LiNi_{0.5}Co_{0.2}Mn_{0.3}O_2$ samples in the voltage range of (a) 2.7 – 4.4 V and (b) 2.7 – 4.6 V, and (c) the corresponding differential capacity (dQ/dV) vs. cell potential profiles based on (b).

The initial charge/discharge curves and the corresponding differential capacity profiles of the pristine and $LiAlO_2$-inlayed $LiNi_{0.5}Co_{0.2}Mn_{0.3}O_2$ materials are showed in Fig. 7. Electrochemical tests have been carried out under 0.1C rate (1C = 180 mA g^{-1}) in the voltage range of 2.7 − 4.4/4.6 V at room temperature. All the charge/discharge curves show a typical potential plateau at 3.75 V. As seen in Fig. 7a, the NMC exhibits superior discharge capacity than that of the $LiAlO_2$-inlayed samples, this is because the $LiAlO_2$ phase is electrochemical inactivity. However, as the voltage range is extended to 2.7 − 4.6 V (Fig. 7b), the initial

discharge capacities for the NMC and $LiAlO_2$-inlayed samples are 205.4, 212.2, 221.3 and 199.7 mAh g^{-1}, with a coulombic efficiency of 81.2%, 84.6%, 87.02% and 78.7%, respectively. In comparison, the materials with $LiAlO_2$ inlaying also show less cell polarization as indicated by dQ/dV curves in Fig. 7c. The lower capacity, poorer coulombic efficiency and larger polarization of NMC sample, compared to that of the LA1 and LA2, can be ascribed to the interface structure deterioration of $LiNi_{0.5}Co_{0.2}Mn_{0.3}O_2$ under high voltage operation (4.6 V).[8, 9] Fortunately, The ultrathin $LiAlO_2$ coating layer could effectively protect the bulk from directly contacting the electrolyte to form inactive NiO layer, and enhance the lithium ion diffusion ability between electrode/electrolyte interface,[40, 41] while the presence of Al in the bulk could also suppress the cation-mixing degree, as reported by Ohzuku et al. and Pouillerie et al.[42, 43]

Fig. 8a compares the rate capability of the pristine and $LiAlO_2$-inlayed $LiNi_{0.5}Co_{0.2}Mn_{0.3}O_2$ samples. The cells were charged/discharged at 0.1C − 5C, and then charged/discharged at 1C in the range of 2.7 − 4.6 V at room temperature. As shown in Fig. 8a, the $LiAlO_2$-inlayed samples show inspiring rate capability than the pristine counterparts at high rates. For example, although the rate capability of LA3 is similar to that of the pristine one at low current density (0.1C − 1C); the former takes the capacity advantage of 59.4% under 5C, compared to the pristine counterpart, which is only 76 mAh g^{-1}. This can be ascribed to the fact that excess Al_2O_3 coating results in suppressing formation of inert layer as well as leads to lower conductivity.[44] In initial lower current stage, excess Al_2O_3 coating affects the conductivity obviously. As the current increases, compared to severe surface deterioration of bare NMC, the coating sample owns much more stable interface for charge transfer.

It is also noted that the LA2 exhibits 202 mAh g^{-1} at 1C and 158.5 mAh g^{-1} at 5C. When cycled at 1C again, the capacity recovery of the pristine and ultrathin $LiAlO_2$-inlayed samples (1 mol% and 2 mol%) is 92.3%, 97.5%, and 97.7%, respectively. These results confirm that the ultrathin $LiAlO_2$ coating is beneficial to the Li^+ intercalation/de-intercalation.[40] The superior rate capability of LA2 can be attributed to the appropriate amount of Al^{3+} ions. For LA1 (Fig. 3f), the coating layer is discontinuous and cannot offer comprehensive protection for cathode particles. For LA3 (Fig. 3h), the $LiAlO_2/Al_2O_3$ nanosheets grow thicker and wider and become harmful to the diffusion of Li^+ ions and electron. Thus, an optimum Al^{3+} ions amount should exist.

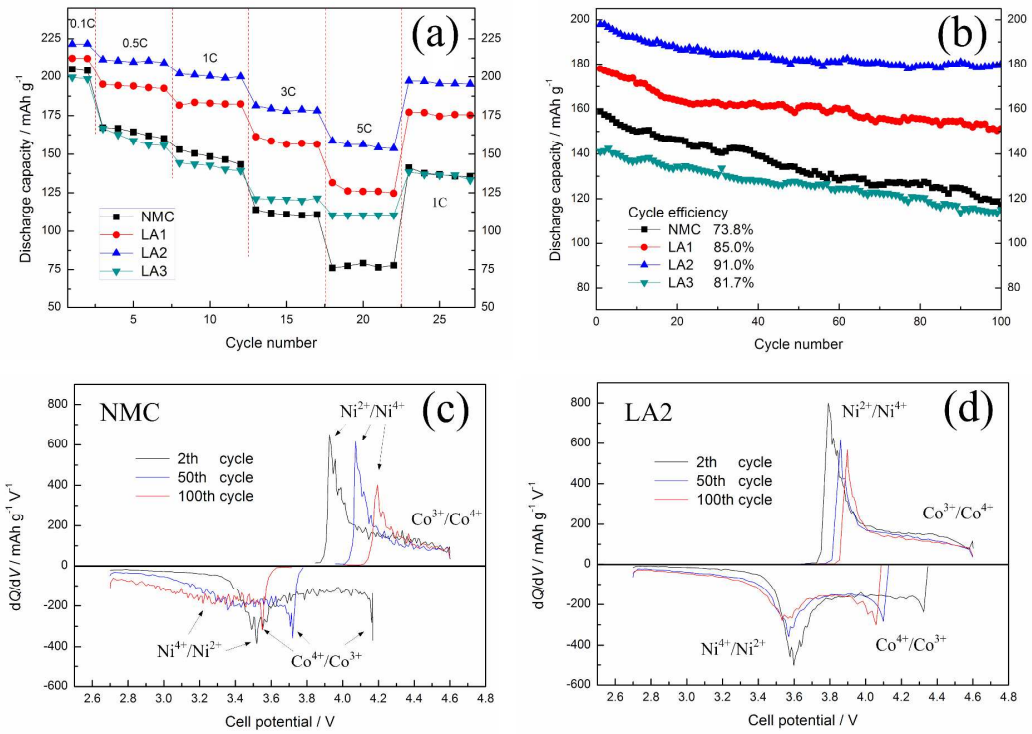

Fig. 8 (a) Rate capability and (b) cyclic performance of pristine and $LiAlO_2$-inlayed $LiNi_{0.5}Co_{0.2}Mn_{0.3}O_2$ samples, and corresponding differential capacity (dQ/dV) vs. cell potential profiles of (c) NMC and (d) LA2 based on (b).

The cycling stability of the pristine and $LiAlO_2$-inlayed $LiNi_{0.5}Co_{0.2}Mn_{0.3}O_2$ materials is given in Fig. 8b. The cells were initially charged at 0.1C, and then discharged and charged at 1C in the voltage of 2.7 − 4.6 V for 100 times. The pristine sample shows fast capacity fading and only 73.8% discharge capacity is left after 100 cycles. Nevertheless, the cycling performance of the layered compounds has been improved significantly by $LiAlO_2$ inlaying, the discharge capacity retention reaches 85%, 91% and 81.7% after 100 cycles for LA1, LA2 and LA3, respectively.

To investigate the evolution of the voltage profile with cycling, differential capacity (dQ/dV) curves are determined for the 2^{th}, 50^{th} and 100^{th} cycles of NMC and LA2 at 1 C rate between 2.7 − 4.6 V. For the NMC (Fig. 8c), the cathodic peaks, identified as Ni^{2+}/Ni^{4+}redox couple, shift from about 3.92 V to 4.07 V and to 4.2 V during cycling. While, the anodic peaks, identified as Co^{4+}/Co^{3+} redox, shift from about 4.19 V to 3.7 V and to 3.55 V during cycling.

Both represent great cell polarization of NMC. Moreover, the anodic peaks, identified as Ni^{4+}/Ni^{2+} at 3.52 V for the second cycle has been broadened and weakened after 100 cycles, which should be ascribed for the deterioration of the electrode/electrolyte interface and the continuous transformation and accumulation of inactive NiO. For the LA2 (Fig. 8d), in comparison, the better preserved intercalation/de-intercalation peaks and less cell polarization are evidences for the excellent cycling performance of LA2, which can be mainly attributed to the protection of ultrathin $LiAlO_2$ coating layer and the enhanced structure stability raised by Al doping. Besides, the inlayed structure can also strength the bonding between the coating layer and the bulk, due to the gradient distribution of Al^{3+} ions.[5]

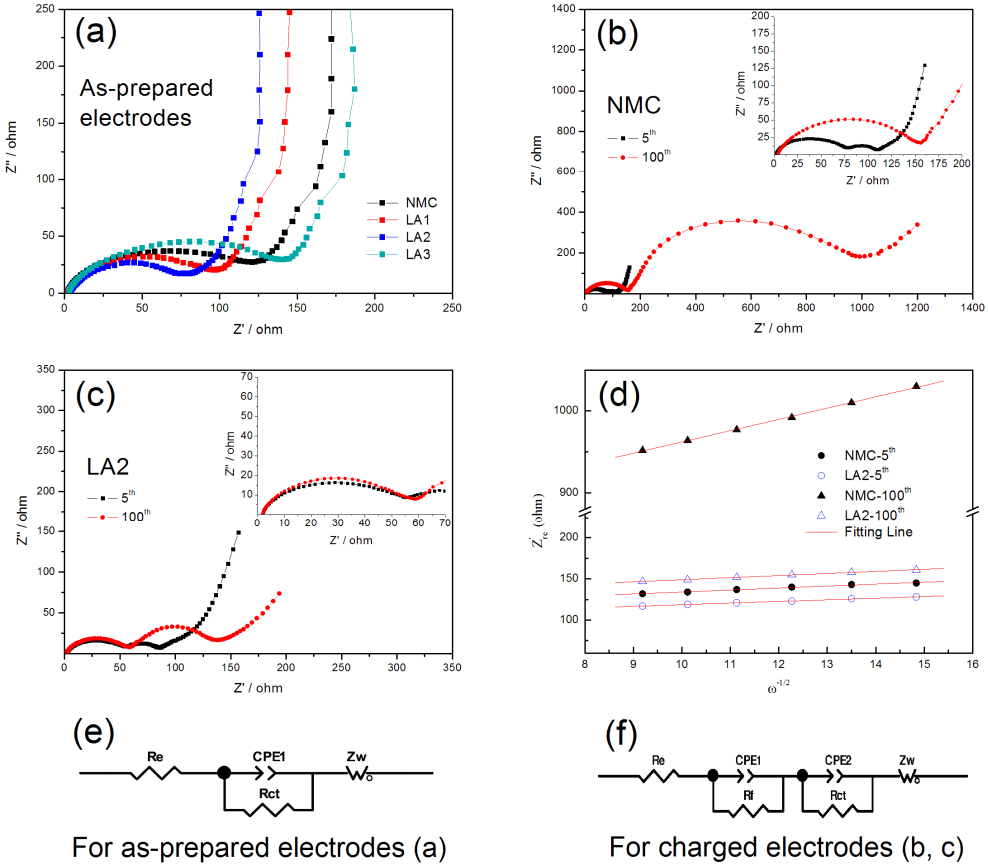

Fig. 9 Nyquist plots of (a) as-prepared electrodes before cycling, (b) NMC and (c) LA2 electrodes at the charge state of 4.4 V after the 5th and 100th cycle. (d) The relationships between Z'_{re} and $\omega^{-1/2}$ based on the 5th and 100th cycle. (e) and (f) Equivalent circuit models used for fitting the experimental EIS data.

To further understand the positive effect of $LiAlO_2$ inlaying on resistance and Li ions transportation, the electrochemical impedance spectroscopy (EIS) and corresponding relationships between Z'_{re} and $\omega^{-1/2}$ are conducted for as-prepared and cycled electrodes in Fig. 9. Fig. 9a presents the Nyquist plots of the as-prepared NMC and $LiAlO_2$-inlayed $LiNi_{0.5}Co_{0.2}Mn_{0.3}O_2$ electrodes. The semicircle at high frequencies represents charge transfer resistance. Whereas, the sloping line at low frequencies represents Warburg resistance, which is directly related to Li^+ diffusion in bulk electrode. The lithium-ion diffusion coefficient can be calculated using following equation.[45]

$$D_{Li^+} = \frac{R^2T^2}{2A^2n^4F^4C^2\sigma^2} \quad (8)$$

Here R is the gas constant (8.314 J K^{-1} mol^{-1}), T is 298 K, F is the Faraday constant (96485 C mol^{-1}), A is the surface area of electrode (0.785 cm^2, considering the surface area of cathode is hardly to be identified), n is the number of electrons involved in reaction, C is the concentration of lithium ion, σ is the Warburg coefficient which can be obtained from the line of $Z'_{re} \sim \omega^{-1/2}$, respectively.

Where the C could be calculated from the density and the molecular weight of the material (as shown in equation 9), x represents the percent of de-intercalated Li at the charge state of 4.4 V. The value of C is 0.0167 mol cm^{-3} in this work.

$$C = (1-x)\frac{n}{V} = (1-x)\frac{(\rho V/M)}{V} = (1-x)\frac{\rho}{M} \quad (9)$$

The Nyquist plots are fitted with the equivalent circuit as show in Fig. 9e and 9f, the values of Rct and D_{Li+} for as-prepared electrodes are exhibited in Table 2 and Table 3, respectively. Due to the fact that the surface area of electrode is larger than that of the cathode, the value of calculated D_{Li+} is smaller than that of real D_{Li+} actually. Besides, in the case of 2-electrode cells the impedance of the cell (Rct) is also the sum of the contributions coming from the cathode and from the anode (Li). However, the calculated D_{Li+} and Rct could still offer some meaningful comparison values and truly reflect the effect of $LiAlO_2$ inlaying on electrochemical kinetics of NMC since all electrodes share same preparation and testing processes, and that these electrodes are assumed to own same thickness and surface area.

Table 2 The values of *R*ct for as-prepared electrodes.

Samples	NMC	LA1	LA2	LA3
*R*ct (±Ω)	102.9	75.24	54.34	118.4

As shown in Table 2, the LA3 exhibits a higher *R*ct value than NMC because of the formation of Al_2O_3 films as confirmed by HRTEM. While the *R*ct value of LA1 and LA2 decrease compared to that of the NMC, which could be ascribed to the removal of amorphous surface Li residues. In particular, the LA2 exhibits the Lowest *R*ct value. These results are consistent to the superior initial charge/discharge performance of $LiAlO_2$-inlayed samples.

Table 3 The values of *R*f, *R*ct and D_{Li+} for cycled electrodes.

Samples	NMC			LA2		
	*R*f (±Ω)	*R*ct (±Ω)	D_{Li+} ($cm^2\ s^{-1}$)	*R*f (±Ω)	*R*ct (±Ω)	D_{Li+} ($cm^2\ s^{-1}$)
5^{th}	71.3	29.9	3.62×10^{-11}	52.5	23.07	5.33×10^{-11}
100^{th}	152.5	707.5	1.10×10^{-12}	55.6	79.22	3.24×10^{-11}

Fig. 9b and 9c illustrate the Nyquist plots of NMC and LA2 samples after the 5^{th} and 100^{th} cycle at the charge state of 4.4 V. A new semicircle is observed in the high frequency range (representing *R*f) of all EIS spectra. The D_{Li+} is calculated by the relationships between Z'_{re} and $\omega^{-1/2}$ at low frequency region shown in Fig 9d. The values of D_{Li+} and fitted EIS results are shown in Table 3. The D_{Li+} value of NMC is 3.62×10^{-11} $cm^2\ s^{-1}$ after 5 cycles, which correspond to the result reported by X.-H. Liu et al.[46]

Additionally, the D_{Li+} values of LA2 samples are higher than that of the NMC, which should be attributed to the fast ion conduction of $LiAlO_2$ and that Al doping enhances the Li ion diffusion coefficient as reported by C. Julien et al.[47]

For the NMC sample, it is obvious that the *R*f and *R*ct values increase dramatically, and the D_{Li+} value decreases more than 10 times after long term cycling. The increased resistance of both electron and Li ions transportation for NMC sample indicates the formation and expansion of inactive surface layers such as LiF and NiO, which are highly related to Li residues on

particles surface.[34] For LA2, in comparison, the *R*f value increases only 3.1 Ω during cycling, which confirms a stable surface film after $LiAlO_2$ ultrathin coating. In addition, the *R*ct value attains 79.22 Ω after 100 cycles, about 11% of that for the pristine one, and the D_{Li+} value is 3.6 × 10^{-9} cm^2 s^{-1} after 100 cycles. The stable resistance and Li ions diffusion coefficient during cycling should be attributed to both the removal of Li residues and the complete, ultrathin coating layer.

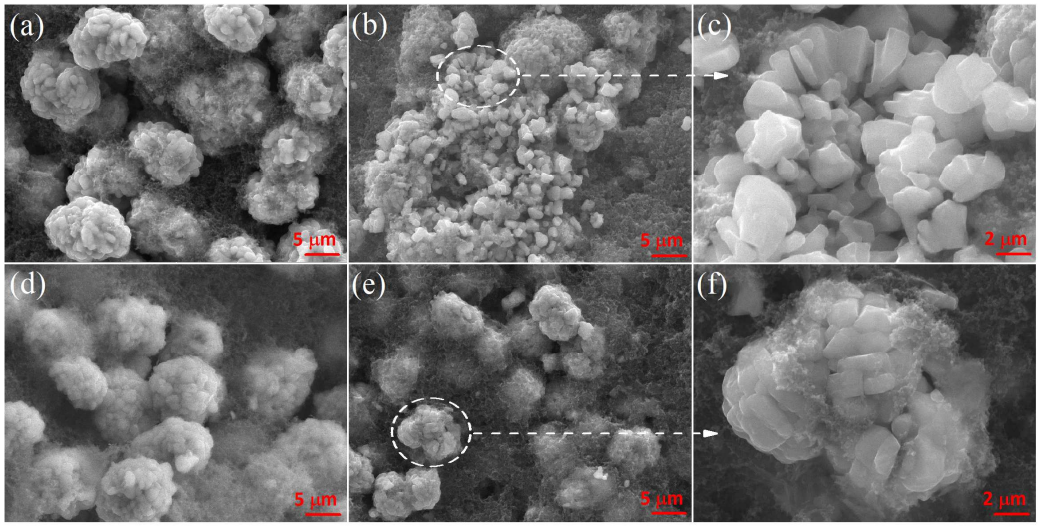

Fig. 10 SEM images of (a, b, c) NMC and (d, e, f) LA2 electrodes, (a and d) before cycling, (b, c, e and f) after 100 cycles at 1 C rate between 2.7 − 4.6 V.

Fig. 10 shows the SEM images of NMC and LA2 electrodes before cycling and after 100 cycles at 1C between 2.7 − 4.6 V. As seen in Fig. 10, compared to the fresh electrodes (Fig. 10 a), the spherical $LiNi_{0.5}Co_{0.2}Mn_{0.3}O_2$ particles suffer serious damage and collapse into many small particles after 100 cycles (Fig. 10b and 10c). This phenomenon can be ascribed to both the HF attack and the oxygen release from the highly delithiated state, which certainly leads to dramatic increase of *R*ct, poor cycling ability and poor thermal stability.[9, 48] In contrast, for LA2, the sphere particle morphology is not changed after 100 cycles, as shown in Fig. 10d, 10e and 10f. The results demonstrate that the $LiAlO_2$-inlayed structure is beneficial to alleviating the damage of HF and retarding the oxygen release by isolating the cathode bulk from the electrolyte.

The schematic illustrations of the unique $LiAlO_2$-inlayed NMC composite and the

modification mechanism are exhibited in Fig. 11. Many reports indicate that the interfacial side reactions and the irreversible structural transition should take responsibility for the capacity fading of NMC.[8, 32] As Seen in equation 10, the Li impurity such as Li_2O could accelerate the decomposition process of $LiPF_6$, release harmful HF and inactive LiF phase.[33, 34] Besides, when charging the NMC, unstable Ni^{4+} is reduced to a divalent and insulating NiO phase at the particle surface, resulting in high interfacial cell impedance and poor electrochemical performance.[9]

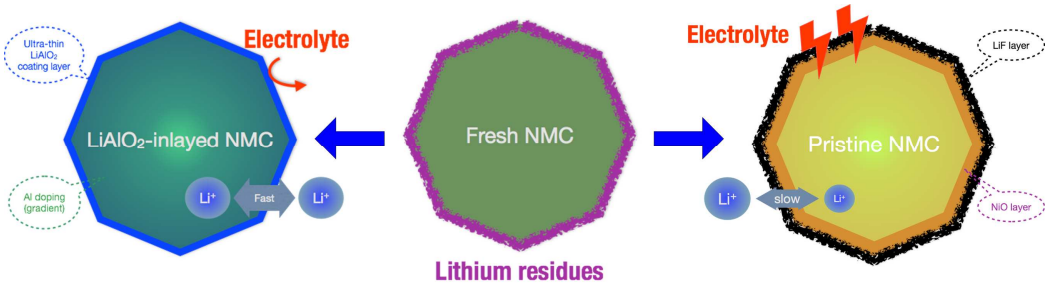

Fig. 11 Scheme illustrations of the $LiAlO_2$-inlayed NMC and its function as a hierarchical protection skin to suppress unwanted side reactions.

$$LiPF_6 + H_2O + Li_2O^- \longrightarrow 2HF + LiF\downarrow + 3Li_xPOF_y \quad (10)$$

The schematic illustrations of the unique $LiAlO_2$-inlayed NMC composite and the modification mechanism are exhibited in Fig. 11. Many reports indicate that the interfacial side reactions and the irreversible structural transition should take responsibility for the capacity fading of NMC.[8, 32] As Seen in equation 10, the Li impurity such as Li_2O could accelerate the decomposition process of $LiPF_6$, release harmful HF and inactive LiF phase.[33, 34] Besides, when charging the NMC, unstable Ni^{4+} is reduced to a divalent and insulating NiO phase at the particle surface, resulting in high interfacial cell impedance and poor electrochemical performance.[9]

In this work, the Li residues are consumed as raw materials to synthesis the complete, ultrathin and crystalline $LiAlO_2$ coating film. The absence of Li impurities is helpful to retard the decomposition of $LiPF_6$ on particle surface and could also prevent the appearance of inactive LiF phase, especially at high voltage operation (4.6 V). The ultrathin $LiAlO_2$ coating film protects the bulk from directly contacting the electrolyte to form inactive NiO layer and enable short diffusion route for both electron and Li^+ ions. Moreover, unlike traditional coatings

which mainly focus on particle surface, the inlayed $LiAlO_2$ structure is also beneficial to the stabilization of host structure, buffering the different volume change of core and shell during de-intercalation of lithium ions and offering a 3D path for Li^+ diffusing from the bulk to interface to reduce the energy barriers for Li^+ ion insertion.[40, 41]

4. Conclusion

In summary, ultrathin $LiAlO_2$-inlayed $LiNi_{0.5}Co_{0.2}Mn_{0.3}O_2$ composites are successfully synthesized via a novel hydrolysis-hydrothermal approach. The prepared $LiAlO_2$-inlayed sample exhibits excellent reversible capacity, enhanced cycling ability and rate capability at high cut-off voltage, compared to the pristine one. This improvement can be ascribed to the removal of lithium residues and the unique inlayed architecture. All of these effects make ultrathin $LiAlO_2$-inlayed $LiNi_{0.5}Co_{0.2}Mn_{0.3}O_2$ a promising cathode material for lithium ion battery, and the hydrolysis-hydrothermal approach could also be extended to other novel structures.

Acknowledgements

This work was financially supported by the National Natural Science Foundation of China (No. 51304031), the Hunan Provincial Natural Science Foundation of China (No. 14JJ3089) and Scientific Research Fund of Hunan Provincial Education Department (No. 12C0001).

References

[1] J.-M. Tarascon, M. Armand, *Nature*, 2001, **414,** 359.

[2] B. Scrosati, J. Garche, *J. Power Sources*, 2010, **195**, 2419.

[3] J.B. Goodenough, Y. Kim, *Chem. Mater.*, 2010, **22**, 587.

[4] M. Guilmard, C. Pouillerie, L. Croguennec, C. Delmas, *Solid State Ionics*, 2003, **160**, 39.

[5] Y.-K. Sun, S. T. Myung, B. C. Park, J. Prakash, I. Belharouak and K. Amine, *Nat. Mater.*, 2009, **8**, 320.

[6] M. Noh, J. Cho, *J. Electrochem. Soc.*, 2013, **160**, A105.

[7] J. Shu, R. Ma, L. Shao, M. Shui, K. Wu, M. Lao, D. Wang, N. Long, Y. Ren, *J. Power Sources,* 2014, **245**, 7.

[8] J. R. Dahn, E. Fuller, M. Obrovac, U. Vonsacken, *Solid State Ionics*, 1994, **69**, 265.

[9] I. Belharouak, W. Lu, D. Vissers, K. Amine, *Electrochem. Commun.*, 2006, **8**, 329.

[10] J. Eom, M. G. Kim, J. Cho, *J. Electrochem. Soc.*, 2008, **155**, A239.

[11] J. Kim, Y. Hong, K. S. Ryu, M. G. Kim, J. Cho, *Electrochem. Solid State Lett.*, 2006, **9**, A19.

[12] T. Ohzuku, A. Ueda, *J. Electrochem. Soc.*, 1994, **141**, 2972.

[13] J. Cho, G. Kim, H. S. Lim, *J. Electrochem. Soc.*, 1999, **146**, 3571.

[14] S.-W. Woo, S.-T. Myung, H. Bang, D.-W. Kim, Y.-K. Sun, *Electrochim. Acta*, 2009, **54**, 3851.

[15] L. Li, Z. Wang, Q. Liu, C. Ye, Z. Chen, L. Gong, *Electrochim. Acta*, 2012, **77**, 89.

[16] M. G. Kim and J. Cho, *J. Mater. Chem.*, 2008, **18**, 5880.

[17] J.-H. Wang, Y. Wang, Y.-Z. Guo, Z.-Y. Ren and C.-W. Liu, *J. Mater. Chem. A*, 2013, **1**, 4879.

[18] B. Huang, X. Li, Z. Wang, H. Guo, L. Shen, J. Wang, *J. Power Sources*, 2014, **252**, 200.

[19] J. Shim, S. Lee, S. Park, *Chem. Mater.*, 2014, **26**, 2537.

[20] J.-Z. Kong, C. Ren, G.-A. Tai, X. Zhang, A.-D. Li, D. Wu, H. Li, F. Zhou, *J. Power Sources*, 2014, **266**, 433.

[21] P. Hou, X. Wang, D. Song, X. Shi, L. Zhang, J. Guo, J. Zhang, *J. Power Sources*, **265**, 2014, 174.

[22] H. Liu, Y. Yang, J. Zhang, *J. Power Sources*, 2006, **162**, 644.

[23] K. Yang, L.-Z. Fan, J. Guo, X. Qu, *Electrochim. Acta*, 2012, **63**, 363.

[24] M.Marezio, J. P. Remeika, *J. Chem. Phys.*, 1966, **44**, 3143.

[25] L. Hu, Z. Tang, Z. Zhang, *Mater. Lett.*, 2008, **62**, 2039.

[26] K. Leung, Y. Qi, K. R. Zavadil, Y. S. Jung, A. C. Dillon, A. S. Cavanagh, S. H. Lee, S. M. George, *J. Am. Chem. Soc.*, 2011, **133**, 14741.

[27] A. Garcia, G. Torres-Trevio, A. R. West, *Solid State Ionics,* 1990, **40-41**, Part 1, 13.

[28] M. Jo, M. Noh, P. Oh, Y. Kim, J. Cho, *Adv. Energy Mater.*, 2014, 1301583.

[29] D. Liu, Z. Wang, L. Chen, *Electrochim. Acta*, 2006, **51**, 4199.

[30] H. Cao, B. Xia, Y. Zhang, N. Xu, *Solid State Ionics*, 2005, **176**, 911.

[31] H.-S. Kim, Y. Kim, S.-I. Kim, S.W. Martin, *J. Power Sources*, 2006, **161**, 623.

[32] G. T.-K. Fey, V. Subramanian and J.-G. Chen, *Electrochem. Commun.*, 2001, **3**, 234.

[33] X. Xiong, Z. Wang, H. Guo, Q. Zhang, X. Li, *J. Mater. Chem. A*, 2013, **1**, 1284.

[34] X. Xiong, D. Ding, Y. Bu, Z. Wang, B. Huang, H. Guo, X. Li, *J. Mater. Chem. A*, 2014, **2**, 11691.

[35] A. Wierenga, A.P. Philipse, H.N.W. Lekkerkerker, D. V. Boger, *Langmuir*, 1998, **14**, 55.

[36] S. C. Kuiry, E. Megen, S. D. Patil, S. A. Deshpande, S. Seal, *J. Phys. Chem. B*, 2005, **109**, 3868.

[37] Z. L. Tang, L. F. Hu, Z. T. Zhang, *Int. J. Materials and Product Technology*, 2010, **37**, 263.

[38] K. Shizuka, C. Kiyohara, K. Shima, Y. Takeda, *J. Power Sources*, 2007, **166**, 233.

[39] G. V. Zhuang, G. Chen, J. Shim, X. Song, P. N. Ross, T. J. Richardson, *J. Power Sources*, 2004, **134**, 293.

[40] Q. Y. Wang, J. Liu, A. V. Murugan, A. Manthiram, *J. Mater. Chem.*, 2009, **19**, 4965.

[41] J. Lu, Q. Peng, W. Wang, C. Nan, L. Li, Y. Li, *J. Am. Chem. Soc.*, 2013, **135**, 1649.

[42] T. Ohzuku, A. Ueda, M. Kouguchi, *J. Electrochem. Soc.*, 1995, **142**, 4033.

[43] C. Pouilerie, L. Croguennec, C. Delmas, *Solid State Ionics*, 2000, **132**, 15.

[44] J.-H. Park, J.-H. Cho, S.-B. Kim, W.-S. Kim, S.-Y. Lee, S.-Y. Lee, *J. Mater. Chem.*, 2012, **22**, 12574.

[45] Z. Li, F. Du, X.F. Bie, *J. Phys. Chem. C*, 2010, **114**, 22751.

[46] X.-H. Liu, L.-Q. Kou, T. Shi, K. Liu, L. Chen, *J. Power Sources*, 2014, **267**, 874.

[47] C. Julien, M. A. Camacho-Lopez, M. Lemal, S. Ziolkiewicz, *Mater. Sci. Eng. B*, 2002, **95**, 6.

[48] S.-K. Jung, H. Gwon, J. Hong, K.-Y. Park, D.-H. Seo, H. Kim, J. Hyun, W. Yang, K. Kang, *Adv. Energy Mater.*, 2014, **4**, 1300787.